COMMUNICATIONS PHYSICS

ARTICLE

https://doi.org/10.1038/s42005-019-0256-z OPEN

Ultrasonic nodal chains in topological granular metamaterials

Aurélien Merkel [1,2*] & Johan Christensen [1*]

Three-dimensional (3D) Weyl and Dirac semimetals garner considerable attention in condensed matter physics due to the exploration of entirely new topological phases and related unconventional surface states. Nodal line and ring semimetals, on the other hand, can facilitate 3D band crossings characterized by nontrivial links such as coupled chains and knots that are protected by the underlying crystal symmetry. Experimental complexities and detrimental effects of the spin-orbit interaction, among others, pose great challenges for the advancement that can be overcome with other systems such as bosonic lattices. Here we demonstrate that a 3D mechanical metamaterial made of granular beads hosts multiple intersecting nodal rings in the ultrasonic regime. By unveiling these yet unseen classical topological phases, we discuss the resilience of the associated novel surface states that appear entirely unaffected to the type of crystal termination, making them a promising platform in ultrasonic devices for non-destructive testing and material characterization.

[1] Department of Physics, Universidad Carlos III de Madrid, ES-28916 Leganès, Madrid, Spain. [2] Institut Jean Lamour, Université de Lorraine, CNRS, F-54000 Nancy, France. *email: aurelien.merkel@univ-lorraine.fr; johan.christensen@uc3m.es

Topological phases of matter in insulators and superconductors have recently been extended to semimetals, thus broadening the family of exotic topological states[1,2]. This active frontier in condensed matter physics recently explored topologically protected degeneracies in Dirac and Weyl semimetals that are identified by topologically robust band-touching manifolds. These unconventional fermionic semimetals are characterized by nontrivial band touching in the form of zero-dimensional discrete points, one-dimensional nodal rings and lines, or two-dimensional nodal surfaces. Peculiar topologically protected **k**-space geometrical manifolds appear in various interlaced nodal chains and links whose nontrivial linking carry a toroidal Berry phase of π, provided the loops enclose the aforementioned nodal shapes[3,4].

The nontrivial Berry flux is responsible for the formation of topologically nontrivial surface states that emerge from the intersecting points of nodal shapes. For example, bulk Weyl points give rise to surface Fermi arcs, whereas nodal rings host flat drumhead surface states that are relevant for topologically robust transport. Various materials have been predicted to sustain Dirac or Weyl fermions and contemporary experiments report on the observation of anisotropic or negative magnetoresistance in three-dimensional semimetals[5–9].

As opposed to nodal points and lines, nodal rings can generate exotic intersecting formations in the form of chains, knots and Hopf links that opens new horizons for unprecedented topological properties, unusual surface states and novel physics in general. A vast amount of theory has been devoted to this frontier in Heusler compounds, alkaline earth metals and electrides[7,10–15], whereupon experimental verifications of nodal rings have already been observed in non-centrosymmetric superconducting compounds and zirconium-based structures[16–19].

Bosonic settings such as photonic, phononic, and sonic crystals are widely studied with the aim to tailor classical wave properties[20]. Accordingly, given the complexity of electronic systems to unveil Weyl and Dirac semimetal physics as well as those peculiar intersecting nodal rings, man-made bosonic system have become increasingly popular to explore in the waves based context, the existence of Dirac-like plasmons[21], optical Weyl points and Fermi arcs[22,23], hourglass nodal lines[24], metallic mesh nodal chains[25], and phononic nodal rings[26].

In this work, we present an excerpt of the catalogue of nodal-chain semimetals for classical mechanical waves in man-made granular metamaterials. By solving the equations of motion for these artificial discrete media, we are able to engineer exotic mechanical intersecting nodal rings whose surface states at the truncated lattice interfaces display a remarkable durability.

Results

Interlaced nodal chains in granular metamaterial. The elastic behavior of granular media drastically differs from conventional elastic waves in solids. At frequencies below the first spheroidal resonance of individual beads, the structure is modeled by rigid masses of finite size connected by stiffnesses originating from the contact laws between the beads, thus forming a discrete crystalline lattice. Specifically here, we consider a face centered cubic (FCC) arrangement as illustrated in Fig. 1a. In the general case in the linear approximation, the contact between two grains is described by one shear stiffness K_S, one torsion stiffness G_T, and one bending stiffness G_B accounting for the sliding, twisting, and rolling resistances at the level of the contact, respectively, in addition to the usual normal stiffness K_N as sketched in Fig. 1a. As a consequence, the rotational degrees of freedom of each individual particle play an important role in the dynamics of granular media. The linear equations of motion for one bead α, with its infinitesimal displacement $\mathbf{u}^\alpha$ and angular rotation $\mathbf{w}^\beta$ around its equilibrium position in a monodisperse granular assembly, read for translation

$$m_b \frac{\partial^2 \mathbf{u}^\alpha}{\partial t^2} = \sum_\beta \mathbf{F}^{\beta\alpha}, \tag{1}$$

and for rotation

$$I_b \frac{\partial^2 \mathbf{w}^\alpha}{\partial t^2} = \sum_\beta \mathbf{M}^{\beta\alpha} + \frac{1}{2}\sum_\beta (\mathbf{R}^\beta - \mathbf{R}^\alpha) \times \mathbf{F}^{\beta\alpha}, \tag{2}$$

where the summation of forces $\mathbf{F}^{\beta\alpha}$ and torques $\mathbf{M}^{\beta\alpha}$ take place over all the beads β at the position $\mathbf{R}^\beta$ in contact with the bead α of mass m_b, moment of inertia I_b, and at the position $\mathbf{R}^\alpha$[27,28] (see Methods section). The FCC structure is formed by spheres of radius $r_b = 5$ mm made of stainless steel with Young's modulus $E = 200$ GPa, Poisson's ratio $\nu = 0.3$ and density $\rho_b = 7.7 \cdot 10^3$ kg m^{-3}. The lattice constant of the FCC structure is $a = (2\sqrt{2})r_b$. We assume that the contacts between the particles are formed by a solid bridge with a radius $r_s = r_b/20$ and a length $h_s = r_b/50$. The different stiffnesses are $K_N = \pi E r_s^2/h_s = 3.9 \cdot 10^8$ N m^{-1}, $K_S = K_N/(2+2\nu) = 1.5 \times 10^8$ N m^{-1}, $G_T = K_S r_s^2/2 = 4.7$ N m rad^{-1} and $G_B = K_N r_s^2/4 = 6.1$ N m rad^{-1}[29]. The Bloch bands structure shown in Fig. 1b depict the propagation of a longitudinal (L), rotational (R), two Transverse-Rotational (TR) and two Rotational-Transverse (RT) modes[30]. The influence of the rotational degrees of freedom has been experimentally confirmed in granular assembly with both millimeter-sized spheres[30] and micron-sized spheres[31] showing the wide range of frequencies and size scales where this model remains valid. The RT and R modes are optical-type modes and have no equivalent in continuum elastic solids. Thanks to the existence of these two type of modes, the bulk bands display accidental degeneracies as marked by squares, triangles, diamonds and hexagons in Fig. 1b, c in the highlighted zone around 150 kHz. These degeneracies are accidental because of their dependence on the values of the stiffnesses (see Supplementary Note 1 for greater details). Owing to the symmetries of the lattice that prohibit a gap opening, the band crossings are not discrete in the reciprocal space but extend to nodal rings in the Brillouin zone, as shown in Fig. 1c. The formation of the intersecting nodal rings stems from three types of symmetries, namely the mirror reflection symmetry, the time-reversal along with the space inversion symmetries and the nonsymmorphic group with glide plane or screw axes symmetry[32,33]. On account of the O_h point group symmetry of the FCC lattice, the (001) plane, comprising either the k_x, k_y or $k_z = 0$ planes, is a mirror reflection plane and thus hosts here two overlaying nodal rings with frequencies ranging from 148 to 152 kHz. In the frequency range spanning from 147 to 157 kHz, two nodal rings lie in and are protected by the (110) mirror plane, here shown as the $k_y = k_z$ plane. The high-symmetry direction Γ–X joins the (110) and (001) surfaces, therefore the aforementioned inner nodal chains are interconnected in the form of outer nodal chains at the point marked with an orange square as shown in Fig. 1c[13]. Similarly, the high-symmetry direction Γ–Z also connects these two symmetry planes, thus, these two nodal chains merge again at the point marked with a triangle. The time-reversal symmetry is always preserved in our case, and adding the space inversion symmetry, two concentric nodal rings are protected across the (111) surface, however, slightly off-plane[33]. Since the bands crossings that are marked with orange diamonds and hexagons occur across the L–U and L–K directions that extend onto the (110) plane, the four nodal rings intersect in an interlaced combination of outer nodal chains and a Hopf link.

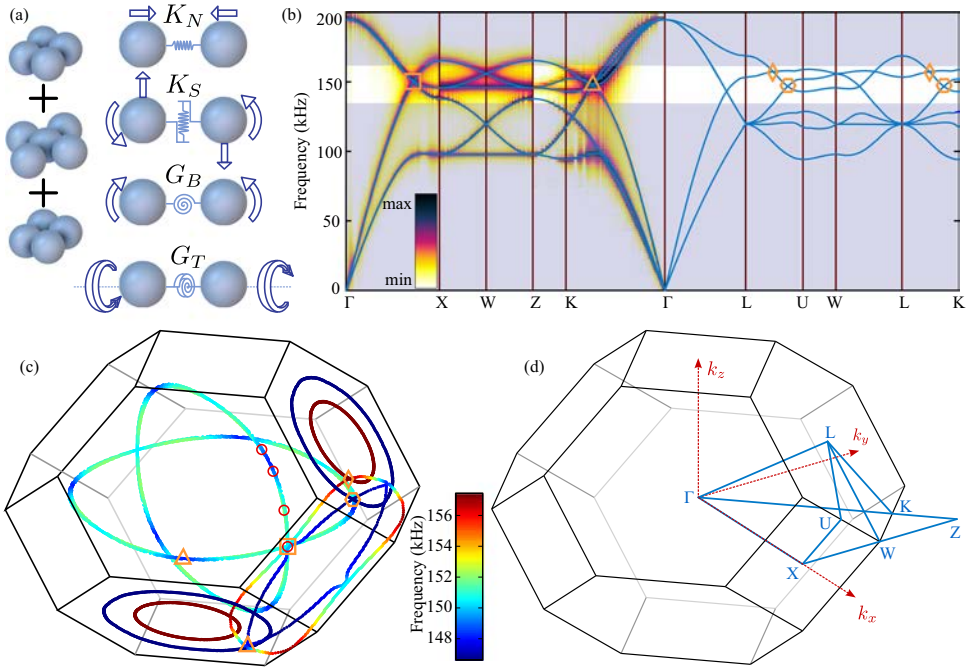

Fig. 1 Band structure of the face centered cubic (FCC) granular metamaterial. **a** Schematic of the structure comprising four different types of interactions between the beads, namely the normal interaction with the stiffness K_N, the interactions due to the sliding, rolling and twisting resistances at the level of the contact with the siffnesses K_S, G_B, and G_T, respectively. **b** Analytical band structure over the entire Brillouin zone shown in (**d**). On the same diagram we numerically compute the dispersion relation for a periodic superlattice (see Methods section). **c** The nodal-chain structure in momentum space evaluated in the ultrasonic frequency regime highlighted in (**b**). The orange squared, triangles, hexagons and diamonds mark the crossing points from the band diagram in (**b**). The red circles show the positions of the nodal lines that are discussed in Fig. 2. **d** The first Brillouin zone of the FCC crystal.

Nontrivial surface states. We now investigate the existence of topologically nontrivial surface states on the (001) plane by means of numerical simulations in a finite FCC granular metamaterial slab, which remains periodic only in the x and y directions but has stress-free boundary conditions at the upper and lower crystal terminations. The numerical simulations are carried out using a Discrete Particle Method with the code MercuryDPM[34–36] and the dispersion bands are found by computing the two-dimensional Fourier transform in time and space along one unique direction[28,37] (see Methods section). In order to unravel these geometrically nontrivial surface excitations in the entire 3D space, we compute them along the usual in-plane components of the wavevector but evaluate the band diagram for various out-of-plane wavevector components k_z. Technically speaking, we implemented this by an emitting bead-array whose phase difference accounts for different wave propagation momenta. The band diagram of the granular metamaterial slab, which is presented in Fig. 2 is characterized by red circles, also seen in Fig. 1c, indicating the dispersion along the rim of the nodal ring at $k_y = 0$. The gray shaded background of the diagrams illustrate the projected bulk bands sustained by the slab containing the stress-free surfaces along the z direction. With seemingly little dispersion with varying out-of-plane momentum k_z, Fig. 2 illustrates the presence of a surface state within the incomplete band gaps that are confined to the nodal ring. Specifically, as rendered by the white dashed area, the bulk band gap spans from 138 to 146 kHz in between which, an entirely flat surface state resides (141 kHz). Further, this surface excitation that transpires from the degenerate bulk states (red circles) with a near zero group velocity, emerges from the nontrivial Berry phase of the nodal rings. In addition, as expected, at lower frequencies trivial surface states that are associated to the stress-free boundary condition are also excited as shown in Fig. 2.

In order to shed light on the topological properties of the surface waves discussed above, we compare three different crystal terminations. In addition to the free boundary condition, we consider the cases where the top layer is in contact with a plane rigid wall and where the top layer is in contact with a layer of fixed (immovable) particles placed in the continuity of the crystalline structure. These three crystal terminations produce an interface between the granular metamaterial and a medium into which sound waves cannot leak. A single chain of excited particles parallel to the y axis acts as the source, hence, all kind of states can be easily excited parallel to the crystal termination for all possible values of k_z. In the numerical experiments, we probe the mechanical response to the excitation in the nearest vicinity of the termination. As one can see in Fig. 3 within the dashed blue ellipses, the trivial surface states at lower frequencies are highly sensitive to the specific boundary condition employed. Beyond significant shifts and enforced dispersion, the trivial surface state ceases to exist in the presence of a fixed crystal termination. On the contrary, the surface state emerging from the nodal rings remains intact and within the bulk band gap in every scenario as highlighted by the black dotted ellipses, underlining its topological origin and resilience against drastic interface perturbations.

The above-mentioned robustness against interface perturbation of the topological surface states emanating the nodal rings is visualized by computing the mechanical motions as shown in Fig. 4. At the ante-penultimate layer we place a source array with a predefined spatial phase profile, as rendered in Fig. 4a, to momentum match ($k_x = 1.9\pi/a$, where a is the lattice constant) the two distinct surface states computed in Fig. 3 at their corresponding frequencies. In Fig. 4b, c we compute the spatial mechanical field of the surface states confined along the stress-free crystal termination. The topological nontrivial (trivial) state at 141 kHz (72 kHz) displays a strong field confinement, it appears however that the low frequency excitation displays a

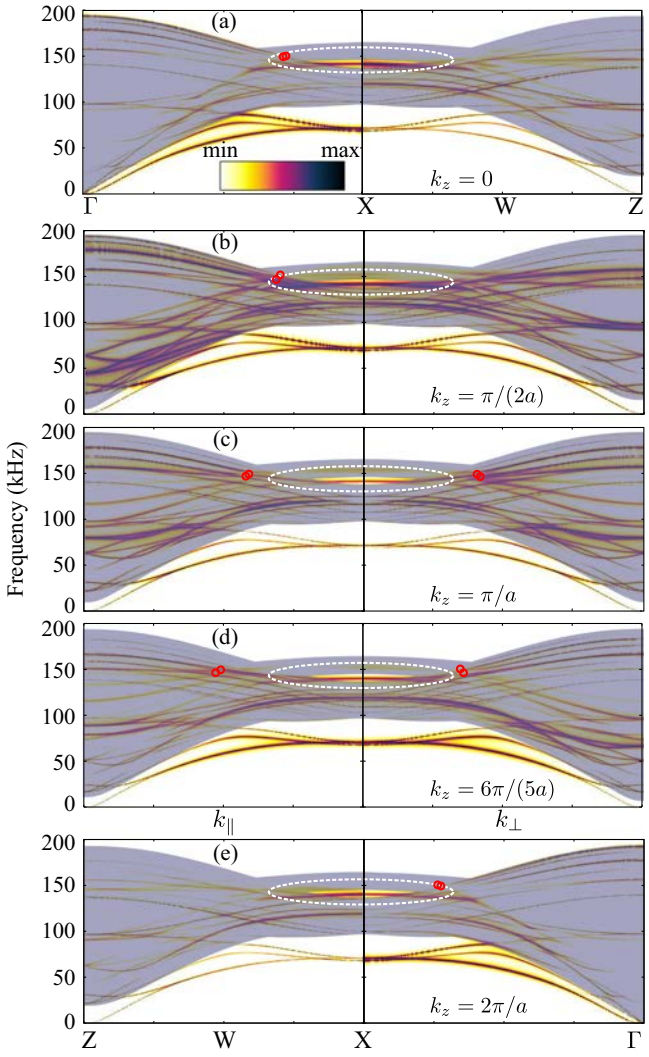

Fig. 2 Topological surface states for the granular metamaterial on the (001) interface. The gray shaded area depict the projected bulk bands. $k_\parallel$ is oriented along the Γ-X direction whereas $k_\perp$ is oriented along the X-Z direction. The white dashed ellipses highlight the topological surface states. The red circles mark the positions of the nodal lines as reported in Fig. 1c. Out-of-plane wavevector component (**a**) $k_z = 0$, (**b**) $k_z = \pi/(2a)$, (**c**) $k_z = \pi/a$, (**d**) $k_z = 6\pi/a$, and (**e**) $k_z = 2\pi/a$.

smaller penetration depth. Finally, we introduce a fixed termination above the top layer. Apart from an unremarkable frequency shift, the mode shape of the confined topological nontrivial surface state at 145 kHz persists virtually unaffected when comparing Fig. 4b, d. With a fixed termination, as computed in Fig. 3, the trivial state ceases to exist, hence at 72 kHz the field remains solely localized around the excitation source as illustrated in Fig. 4e. Additional time resolved computations, which are placed in the Supplementary Movies, display how the source is able to couple to the topological nontrivial states irrespective of the crystal termination. The lifetime of these excitations can be clearly witnessed when the source is switched off. In stark contrast, only source oscillations can be seen in the transient analysis at 72 kHz when a fixed termination is added, confirming the absence of mode propagation.

Discussion

In conclusion, three-dimensional man-made FCC granular metamaterials have been found to host complex structures of nodal rings interlaced in the form of inner and outer chains. The symmetry protected nodal features give rise to remarkably robust surface states that appear entirely unaffected by the type of crystal termination. Hence, our results provide a convincing platform to implement topological nontrivial nodal rings and chains physics for mechanical waves, potentially useful for robust ultrasonic sensing and transduction.

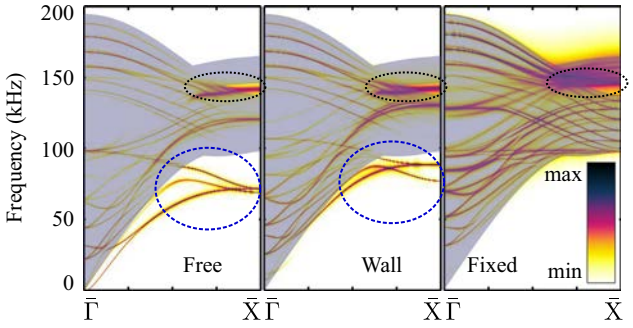

Fig. 3 Ultrasonic band diagram along the $\bar{\Gamma}$-$\bar{X}$ direction of topological surface states in a finite slab. We consider three different crystal terminations: free, in contact with a wall, and fixed. The blue dashed (black dotted) circle mark the spectral region of the topologically trivial (nontrivial) surface states.

Methods

Theoretical calculations. To obtain the force $\mathbf{F}^{\beta\alpha}$ and torque $\mathbf{M}^{\beta\alpha}$ applied by a bead β on a bead α, we define a local coordinate system $(\mathbf{n}, \mathbf{s}, \mathbf{t})$ at the level of the contact between the two beads. In Cartesian coordinates the unit vector $\mathbf{n}$, normal to the contact surface, is defined as

$$\mathbf{n} = (\mathbf{R}^\beta - \mathbf{R}^\alpha)/|\mathbf{R}^\beta - \mathbf{R}^\alpha| = \cos\phi\hat{\mathbf{x}} + \sin\phi\cos\theta\hat{\mathbf{y}} + \sin\phi\sin\theta\hat{\mathbf{z}}, \quad (3)$$

where it is assumed that the static and dynamic overlap between the particles are negligible compared to their diameter, $\phi = \arccos(\mathbf{n}\cdot\hat{\mathbf{x}})$, $\theta = \arccos(\mathbf{n}\cdot\hat{\mathbf{y}}/\sin\phi)$ if $\phi \neq 0$ or π and $\theta = \phi$ if $\phi = 0$ or π. The two unit vectors $\mathbf{s}$ and $\mathbf{t}$, which are in the contact plane, are then defined as

$$\begin{aligned}\mathbf{s} &= \partial\mathbf{n}/\partial\phi = -\sin\phi\hat{\mathbf{x}} + \cos\phi\cos\theta\hat{\mathbf{y}} + \cos\phi\sin\theta\hat{\mathbf{z}},\\ \mathbf{t} &= \mathbf{n}\times\mathbf{s} = -\sin\theta\hat{\mathbf{y}} + \cos\theta\hat{\mathbf{z}}.\end{aligned} \quad (4)$$

The contact force is then written as[27,28]

$$\begin{aligned}F_i^{\beta\alpha} = &\left[K_N n_i n_j + K_S(s_i s_j + t_i t_j)\right]\\ &\times\left[u_j^\beta - u_j^\alpha + \frac{1}{2}\varepsilon_{jkl}(R_k^\beta - R_k^\alpha)(w_l^\beta + w_l^\alpha)\right],\end{aligned} \quad (5)$$

where ε_{jkl} is the permutation symbol, and the contact torque is expressed as

$$M_i^{\beta\alpha} = \left[G_T n_i n_j + G_B(s_i s_j + t_i t_j)\right]\left(w_j^\beta - w_j^\alpha\right). \quad (6)$$

Our FCC structure is formed by spheres of radius $r_b = 5$ mm, which are composed of stainless steel with a Young modulus $E = 200$ GPa, Poisson's ratio $\nu = 0.3$ and density $\rho_b = 7.7\cdot 10^3$ kg m^{-3}. The lattice constant of the FCC structure is $a = (2\sqrt{2})r_b$. We assume that the contacts between the particles are formed by a solid bridge with a radius $r_s = r_b/20$ and a length $h_s = r_b/50$. The different stiffnesses are determined as[29]

$$\begin{aligned}K_N &= \pi E r_s^2/h_s = 3.9\times 10^8\ \mathrm{N\,m^{-1}},\\ K_S &= K_N/(2+2\nu) = 1.5\times 10^8\ \mathrm{N\,m^{-1}},\\ G_T &= K_S r_s^2/2 = 4.7\ \mathrm{N\,m\,rad^{-1}},\ \text{and}\\ G_B &= K_N r_s^2/4 = 6.1\ \mathrm{N\,m\,rad^{-1}}.\end{aligned} \quad (7)$$

The two stiffnesses G_T and G_B contain a length scale i.e., $G_T = K_T r_b^2$ and $G_B = K_B r_b^2$. The crystalline structure is constructed using the three Bravais lattice vectors

$$\begin{aligned}\mathbf{a}_1 &= [a/2, 0, a/2],\\ \mathbf{a}_2 &= [a/2, a/2, 0],\\ \mathbf{a}_3 &= [0, a/2, a/2].\end{aligned} \quad (8)$$

The position of the bead (l, m, p) is defined as $\mathbf{R}^{(l,m,p)} = l\mathbf{a}_1 + m\mathbf{a}_2 + p\mathbf{a}_3$, where l, m and p are integer indices.

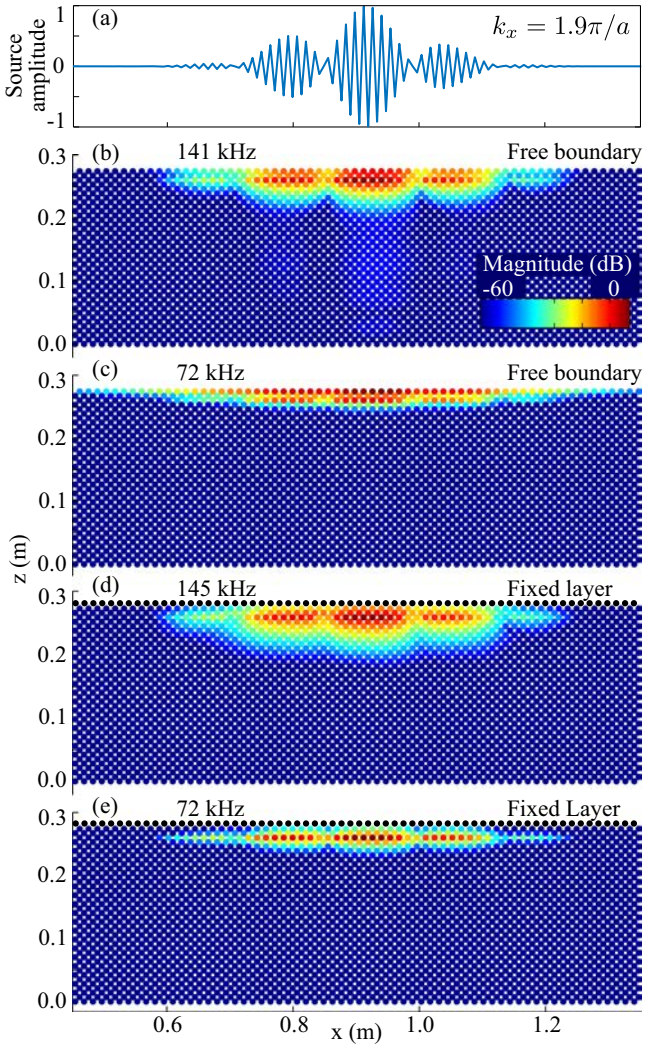

Fig. 4 Launching of surface states parallel to the terminated crystal interface (001) (along the Γ-X direction) by placing a harmonic source at the ante-penultimate layer. **a** Spatial source profile to momentum match, $k_x = 1.9\pi/a$, the trivial (72 kHz) and nontrivial (141 kHz and 145 kHz) surface states. **b**–**e** Total velocity magnitudes of the Fourier transformed linear $\mathbf{v} = d\mathbf{u}/dt$ and angular velocity $r_b\mathbf{W} = r_b d\mathbf{w}/dt$. (**b**, **d**) Nontrivial surface state with a stress-free termination and a fixed (clamped) termination. **c** Conventional or trivial surface wave with a stress-free termination. **e** Fixed termination, here no trivial surface state exists.

Numerical simulations. The numerical simulations are carried out using a Discrete Particle Method (or Discrete Element Method) with the code MercuryDPM[34–36], to calculate the time integration of the equations of motion in Eqs. (1) and (2) using a Verlet velocity algorithm on an assembly of grains.

The crystal is constructed using the Bravais lattice vectors in Eq. (8) and the different stiffnesses between the beads are the ones in Eq. (7). The cohesive character induced by the solid bridges is emulated by adding an attractive force between the beads. The friction coefficient is set to an arbitrarily large value to avoid any slip event at the level of the contacts. Periodic boundary conditions are applied along all directions in Fig. 1b and solely along the x and y directions in Figs. 2–4.

The dispersion bands are found by computing the two-dimensional Fourier transform in time and space along one unique direction[28,37]. When the Fourier transform is computed along the x direction, the corresponding band diagram is displayed along the k_x component of the wavevector as in Fig. 1b for the Γ–X path of the Brillouin zone, shown on the left panels in Fig. 2 and in Fig. 3. In this direction, P layers are stacked. The numbers of particles within each of these layers is $N_b = N \times M/2$, where N is the number of layers in the y direction and M is the number of layers along the z direction. In Fig. 1b and Fig. 2a–c and e, $P = 512$, $N = 8$ and $M = 8$. In Fig. 2d, $P = 512$, $N = 8$ and $M = 10$. In Fig. 3, $P = 1024$, $N = 8$ and $M = 8$. At the first time step of the numerical simulation, an acoustic wave is launched by imposing a (small) velocity and angular velocity, i.e., corresponding to a pulse excitation in time to beads arrayed parallel to the y axis. In doing this, a broad spectrum of frequencies and k_x components of the wavevector are emitted. The others components of the wavevector can be chosen by imposing one specific spatial source profile. On the left panels in Fig. 2, $k_y = 0$, thus, the spatial phase profile of the source allows one to momentum match the corresponding k_z components. In Fig. 3, the source is positioned at the top layer to excite waves in the $k_x - k_z$ plane.

Equivalently, in Fig. 1b for the X–Z path of the Brillouin zone and on the right panels in Fig. 2, $k_x = 2\pi/a$ and the Fourier transform is computed along the y direction to obtain the k_y component of the band diagram. In the y direction, P layers are stacked. The numbers of particles within each of these layers is $N_b = N \times M/2$, where N is the number of layers in the x direction and M is the number of layers along the z direction. The values of P, N, and M in Fig. 1b and Fig. 2 are equal to their counterparts when the Fourier transform is computed in the x direction.

In Fig. 3, the wall termination is obtained by connecting all the beads of the top layer to a plane surface. The stiffnesses of these connections are $K_N^{wall} = K_N$, $K_S^{wall} = K_S$, $G_B^{wall} = G_B$ and $G_T^{wall} = 100G_T$. For the fixed boundary condition, the stiffnesses between the top layer and the layer of fixed particles are equal to the ones in Eq. (7).

In Fig. 4, the source layer is excited by a sine function at the specific frequencies, as indicated in the panels with a Gaussian envelope modulation. The amplitudes are obtained by Fourier transforming the time signals at each individual bead. The slab contains 256 layers in the x direction, 8 layers in the y direction and 40 layers in the z direction.

Data availability

The data that support the findings of this study are available from the corresponding authors on reasonable request.

Received: 19 July 2019; Accepted: 15 November 2019;
Published online: 06 December 2019

References

1. Qi, X.-L. & Zhang, S.-C. Topological insulators and superconductors. *Rev. Mod. Phys.* **83**, 1057–1110 (2011).
2. Armitage, N. P., Mele, E. J. & Vishwanath, A. Weyl and dirac semimetals in three-dimensional solids. *Rev. Mod. Phys.* **90**, 015001 (2018).
3. Burkov, A. A., Hook, M. D. & Balents, L. Topological nodal semimetals. *Phys. Rev. B* **84**, 235126 (2011).
4. Bzdusek, T., Wu, Q., Ruegg, A., Sigrist, M. & Soluyanov, A. A. Nodal-chain metals. *Nature* **538**, 75 (2016).
5. Huang, X. et al. Observation of the chiral-anomaly-induced negative magnetoresistance in 3D weyl semimetal TaAs. *Phys. Rev. X* **5**, 031023 (2015).
6. Arnold, F. et al. Negative magnetoresistance without well-defined chirality in the weyl semimetal TaP. *Nat. Commun.* **7**, 11615 (2016).
7. Schoop, L. M. et al. Dirac cone protected by non-symmorphic symmetry and three-dimensional dirac line node in ZrSiS. *Nat. Commun.* **7**, 11696 (2016).
8. Wang, X. et al. Evidence of both surface and bulk dirac bands and anisotropic nonsaturating magnetoresistance in ZrSiS. *Adv. Electron. Mater.* **2**, 1600228 (2016).
9. Hong, G.-H. et al. Measurement of the bulk and surface bands in dirac line-node semimetal ZrSiS. *Chin. Phys. B* **27**, 017105 (2018).
10. Chen, W., Lu, H.-Z. & Hou, J.-M. Topological semimetals with a double-helix nodal link. *Phys. Rev. B* **96**, 041102 (2017). (R).
11. Yan, Z. et al. Nodal-link semimetals. *Phys. Rev. B* **96**, 041103 (2017). (R).
12. Bi, R., Yan, Z., Lu, L. & Wang, Z. Nodal-knot semimetals. *Phys. Rev. B* **96**, 201305 (2017). (R).
13. Chang, G. et al. Topological hopf and chain link semimetal states and their application to co_2MnGa. *Phys. Rev. Lett.* **119**, 156401 (2017).
14. Gong, C., Xie, Y., Chen, Y., Kim, H.-S. & Vanderbilt, D. Symmorphic intersecting nodal rings in semiconducting layers. *Phys. Rev. Lett.* **120**, 106403 (2018).
15. Hirayama, M., Matsuishi, S., Hosono, H. & Murakami, S. Electrides as a new platform of topological materials. *Phys. Rev. X* **8**, 031067 (2018).
16. Bian, G. et al. Topological nodal-line fermions in spin-orbit metal $PbTaSe_2$. *Nat. Commun.* **7**, 10556 (2016).
17. Neupane, M. et al. Observation of topological nodal fermion semimetal phase in ZrSiS. *Phys. Rev. B* **93**, 201104 (2016). (R).
18. Hu, J. et al. Evidence of topological nodal-line fermions in ZrSiSe and ZrSiTe. *Phys. Rev. Lett.* **117**, 016602 (2016).

19. Lou, R. et al. Experimental observation of bulk nodal lines and electronic surface states in ZrB_2. *NPJ Quantum Mater.* **3**, 43 (2018).
20. Zhang, X., Xiao, M., Cheng, Y., Lu, M.-H. & Christensen, J. Topological sound. *Nat. Commun. Phys.* **1**, 97 (2018).
21. Weick, G., Woollacott, C., Barnes, W. L., Hess, O. & Mariani, E. Dirac-like plasmons in honeycomb lattices of metallic nanoparticles. *Phys. Rev. Lett.* **110**, 106801 (2013).
22. Lu, L. et al. Experimental observation of weyl points. *Science* **349**, 622–624 (2015).
23. Noh, J. et al. Experimental observation of optical weyl points and fermi arc-like surface states. *Nat. Phys.* **13**, 611 (2017).
24. Xia, L. et al. Observation of hourglass nodal lines in photonics. *Phys. Rev. Lett.* **122**, 103903 (2019).
25. Yan, Q. et al. Experimental discovery of nodal chains. *Nat. Phys.* **14**, 461 (2018).
26. Deng, W. et al. Nodal rings and drumhead surface states in phononic crystals. *Nat. Commun.* **10**, 1769 (2019).
27. Merkel, A., Tournat, V. & Gusev, V. Dispersion of elastic waves in three-dimensional noncohesive granular phononic crystals: properties of rotational modes. *Phys. Rev. E* **82**, 031305 (2010).
28. Merkel, A. & Luding, S. Enhanced micropolar model for wave propagation in ordered granular materials. *Int. J. Solids Struct.* **106-107**, 91–105 (2017).
29. Brendel, L., Török, J., Kirsch, R. & Bröckel, U. A contact model for the yielding of caked granular materials. *Gran. Mat.* **13**, 777–786 (2011).
30. Merkel, A., Tournat, V. & Gusev, V. Experimental evidence of rotational elastic waves in granular phononic crystals. *Phys. Rev. Lett.* **107**, 225502 (2011).
31. Hiraiwa, M. et al. Complex contact-based dynamics of microsphere monolayers revealed by resonant attenuation of surface acoustic waves. *Phys. Rev. Lett.* **116**, 198001 (2016).
32. Yu, R., Wu, Q., Fang, Z. & Weng, H. From nodal chain semimetal to weyl semimetal in HfC. *Phys. Rev. Lett.* **119**, 036401 (2017).
33. Hirayama, M., Okugawa, R., Miyake, T. & Muramaki, S. Topological dirac nodal lines and surface charges in fcc alkaline earth metals. *Nat. Commun.* **8**, 14022 (2017).
34. Thornton, A., Weinhart, T., Luding, S. & Bokhove, O. Modeling of particle size segregation: Calibration using the discrete particle method. *Int. J. Mod. Phys. C.* **23**, 1240014 (2012).
35. Weinhart, T., Thornton, A., Luding, S. & Bokhove, O. From discrete particles to continuum fields near a boundary. *Gran. Mat.* **14**, 289–294 (2012).
36. http://www.mercurydpm.org.
37. Mouraille, O., Mulder, W. A. & Luding, S. Sound wave acceleration in granular materials. *Theory Exp.* **2006**, P07023 (2006).

Acknowledgements

J.C. acknowledges the support from the European Research Council (ERC) through the Starting Grant No. 714577 PHONOMETA and from the MINECO through a Ramón y Cajal grant (Grant No. RYC-2015-17156).

Author contributions

J.C. conceived the original idea. A.M. developed the theoretical calculations and performed the numerical simulations. Both authors contributed to the analysis and preparation of the manuscript.

Competing interests

The authors declare no competing interests.

Additional information

Supplementary information is available for this paper at https://doi.org/10.1038/s42005-019-0256-z.

Correspondence and requests for materials should be addressed to A.M. or J.C.

Reprints and permission information is available at http://www.nature.com/reprints

Publisher's note Springer Nature remains neutral with regard to jurisdictional claims in published maps and institutional affiliations.

Open Access This article is licensed under a Creative Commons Attribution 4.0 International License, which permits use, sharing, adaptation, distribution and reproduction in any medium or format, as long as you give appropriate credit to the original author(s) and the source, provide a link to the Creative Commons license, and indicate if changes were made. The images or other third party material in this article are included in the article's Creative Commons license, unless indicated otherwise in a credit line to the material. If material is not included in the article's Creative Commons license and your intended use is not permitted by statutory regulation or exceeds the permitted use, you will need to obtain permission directly from the copyright holder. To view a copy of this license, visit http://creativecommons.org/licenses/by/4.0/.

© The Author(s) 2019